Multiexciton complexes in InAs self-assembled quantum dots

M. Korkusinski, M. Zielinski, and P. Hawrylak[a)]
Institute for Microstructural Sciences, National Research Council, Ottawa K1A 0R6, Canada

(Received 22 January 2009; accepted 27 February 2009; published online 18 June 2009)

We review our recent work on multiexciton complexes in InAs self-assembled quantum dots using a combination of effective mass, $k\cdot p$, and atomistic $sp^3s^*d^5$ tight-binding approaches. The single-particle levels from effective mass, $k\cdot p$, and atomistic tight-binding models are used as input into configuration-interaction calculation of multiexciton spectra. We describe the principles of the atomistic approach and apply all these computational tools to illustrate the concept of hidden symmetry as underlying principle in energy levels of multiexciton complexes, optical detection of electron spin polarization, tunneling of holes in quantum dot molecules, and tuning of multiexciton spectra with lateral electric fields for entangled photon pair generation. © *2009 American Institute of Physics*. [DOI: 10.1063/1.3117231]

I. INTRODUCTION

InAs self-assembled quantum dots (SADs) are clusters of indium and arsenic atoms embedded in a solid state environment. Their electronic and optical properties are controlled by their size, shape, composition, patterning of the substrate, and magnetic and electric fields.[1–3] The microscopic theory of the electronic structure of these systems involves millions of atoms and precludes *ab initio* calculations. Another obstacle is the multiscale nature of the problem, involving strain effects on the micron scale and electronic states on the nanometer scale. Despite these difficulties a significant progress has been achieved using approximate methods. The multiexciton complexes in InAs SADs have been described using a combination of effective mass,[1–3] $k\cdot p$,[1–3] atomistic tight-binding[4–9] and pseudopotential methods,[10,11] allowing computation of the single-particle states and the configuration-interaction approach accounting for the Coulomb interactions between carriers. We describe here several new developments in our understanding of multiexciton complexes. First is the emergence of hidden symmetries, instead of Hund's rules, in the energy levels of multiexciton complexes filling degenerate electronic shells. Second is the understanding of how to optically detect spin polarization in quantum dots. Third example, illustrating the importance of the spin-orbit interaction is the tunneling of holes in quantum dot molecules. The fourth case demonstrates the possibility to manipulate the multiexciton complexes, and in particular of the biexciton-exciton cascade, using lateral electric fields. The fifth example is the development of QNANO, a computational platform for quantum properties of semiconductor nanostructures using the atomistic $sp^3s^*d^5$ tight-binding model coupled to the configuration-interaction tool for the computation of excited states and optical and electronic properties of SADs. The main focus here will be on the description of QNANO.

A. Hidden symmetry

As shown using the atomistic approach (discussed below) and demonstrated experimentally,[12] electronic states in SADs form degenerate electronic shells. Filling of the degenerate shells with electrons and holes is governed by interactions. Through a number of theoretical and experimental papers[13,14] an understanding emerges of how the spin and angular momentum of the ground state of the *N*-exciton complex evolves as a function of the filling of such a shell. For electrons in atomic shells this process is governed by Hund's rules. For electrons and holes in artificial atoms, on the other hand, we deal with a new set of rules developed by us and referred to as "hidden symmetries." Their two main consequences are: (i) the emission energy from a degenerate shell is almost independent of the filling of this shell and (ii) the total spin of the exciton complex is minimized, i.e., two excitons on a doubly degenerate shell form a singlet-singlet state, while the two electrons would form a triplet state. These two rules are illustrated in Fig. 1.

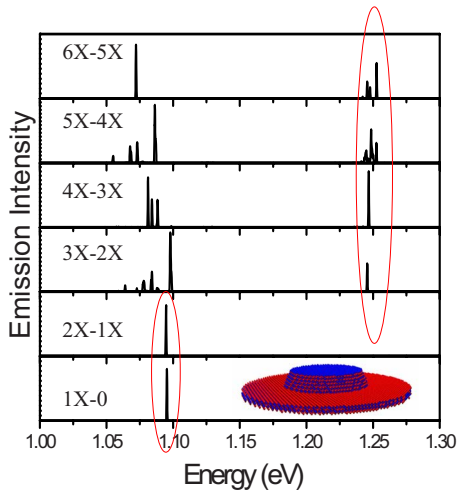

FIG. 1. (Color online) Emission spectra as a function of the filling of the *s* and *p* shells of InAs quantum dot grown by the indium-flush method. The emission spectra insensitive to the filling of degenerate shells due to hidden symmetries are circled.

[a)]Electronic mail: pawel.hawrylak@nrc-cnrc.gc.ca.

B. Optical detection of spin polarization

Recent experiments involving SADs combined with spin-polarized electrical and optical injection demonstrate that the hidden symmetries can be overruled by filling the degenerate shells with spin-polarized carriers. We have investigated theoretically the emission spectra from SADs as a function of spin polarization of excitonic complexes using the effective mass-configuration-interaction approach.[15] We mapped out these spectra as a function of increasing electron spin polarization for a fixed number of electrons and holes. In each case the spin of the holes was not fixed. The ground state of the system was established by comparing the energies of the states of N excitons with given spin of electrons and all possible hole spins. We predicted that the spin polarization leads to photon polarization, to redshifts of emission lines due to excess exchange interactions among the spin-polarized electrons, and to a complete breakup of emission lines for spin-polarized electronic shells.

We have also developed a detailed theory of the biexciton with spin-polarized electrons and holes. Such a complex can be formed in the process of carrier relaxation during cw excitation of quantum dots. We have identified the emission spectrum of quantum dots characteristic for that complex.[16]

C. Tuning of exciton-biexciton cascade with lateral electric fields

We have recently demonstrated theoretically[17] and experimentally[18] that the photon cascades originating from recombination of multiexciton complexes in SADs can be engineered and tuned by applying an in-plane electric field. We calculated the energies of photons emitted by the biexciton and two linearly polarized excitons as a function of the field, and demonstrated the possibility of engineering their degeneracy. Removal of the biexciton binding energy allows for the cascade of a pair of polarization entangled photons without the need for the removal of the exciton anisotropic exchange splitting. We compared these emission spectra to those of other multiexciton complexes. We demonstrated that the electric field and Coulomb interactions differentiate the biexciton-exciton cascade from other cascades, facilitating identification of its spectra and practical implementation.

D. Tunneling of holes in quantum dot molecules

We have shown recently that the strong spin-orbit coupling of the valence band introduces characteristic features in the tunneling of holes, which are not captured by the usual single-band heavy hole approximation.[19,20] Thus, the holes must be treated as Luttinger spinors, and the mixing of valence subbands is responsible for breaking of the parity symmetry in the vertical direction and for introduction of a new chirality symmetry. As a consequence, with increasing inter-dot distance, the spin-orbit interaction leads to a bonding-antibonding ground-state transition of the hole levels. This transition should be observable in emission spectra as a quenching of the exciton peak due to the loss of oscillator strength of the ground-state exciton.

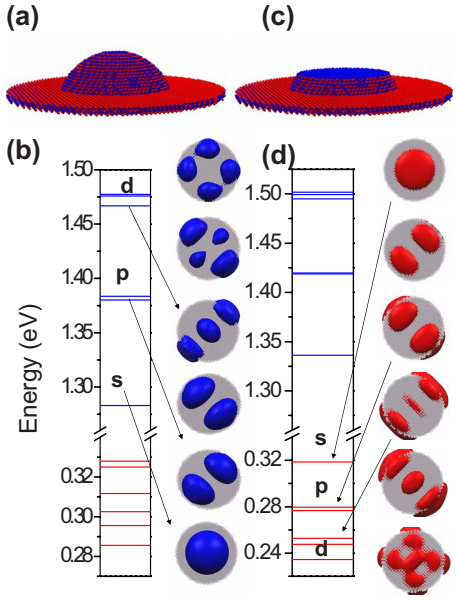

FIG. 2. (Color online) (a) InAs lens-shaped quantum dot embedded in GaAs matrix (only indium and arsenic atoms are shown). (b) Electron probability density isosurfaces and electron and hole energies for dot (a). No shell structure visible for holes. (c) InAs quantum dot grown by the indium-flush method. (d) Hole probability density isosurfaces and electron and hole energy shells for dot (c).

II. ATOMISTIC THEORY OF MULTIEXCITON COMPLEXES

In this section we outline QNANO, our computational tool for quantum properties of nanoscale semiconductor structures. As illustration, we apply this tool to the multiexciton states in InAs lens shaped and grown by indium-flush technique[21] dots embedded in GaAs.

A. Structure definition

We define the quantum dot by defining positions of indium, gallium, and arsenic atoms on the zincblende lattice of GaAs. The dimension of the GaAs barrier box surrounding the dot defines the size of the computational domain. Figure 2 shows examples of two dots: (a) a lens-shaped dot and (c) an indium-flushed dot. The height of the dots is $h=5$ nm for the lens and $h=2$ nm for the indium-flushed dot, and the base diameter in both cases is $D=12.5$ nm. The center of the quantum dot base is an anion arsenic atom. The dot is placed on one lattice constant thick (~ 0.6 nm) wetting layer. At this initial step of calculation all atoms are placed at uniform lattice positions of the bulk barrier (GaAs) material. There are a total of 32.2×10^6 atoms in our computational box.

B. Atomistic calculation of strain

In the next step of the computational procedure we find the equilibrium positions of all the atoms in our computational domain. The necessity of this step is due to the $\sim 7\%$ mismatch between lattice constants of InAs and GaAs. To this end, following Keating,[22] we define the total elastic energy E_{TOT} in terms of the stretching and bending terms of all atomic bonds,

$$E_{\mathrm{TOT}} = \frac{1}{2}\sum_{i=1}^{N}\sum_{j=1}^{n.n.} A_{ij}[(\vec{R}_i - \vec{R}_j)^2 - d_{ij}^2]^2 + \sum_{i=1}^{N}\sum_{j=1}^{n.n.}\sum_{k=j+1}^{n.n.} B_{ijk}\left[(\vec{R}_j - \vec{R}_i)\times(\vec{R}_k - \vec{R}_i) - \frac{1}{3}d_{ij}d_{ik}\right]^2. \quad (1)$$

Here, $\vec{R}_i$ denotes the position of the ith atom, d_{ij} is the bulk bond length between the ith and jth atoms, and A_{ij} and B_{ijk} are material-dependent elastic parameters. The summations go over N atoms and $n.n.$ nearest neighbors. We minimize this total elastic energy with respect to the atomic positions using the conjugate gradient algorithm.

The equilibrium positions of atoms are displaced from those in the bulk, and these displacements, i.e., the lengths and directions of atomic bonds, vary across the sample. As a measure of the displacement field, distribution of strain tensor elements across the sample is then computed by comparing the deformed zincblende unit cells with their unstrained bulk counterparts.[23] Because strain has a long-range character, the GaAs buffer (computational domain) used in the strain energy minimization must be large enough to ensure that the strain fields vanish at the GaAs buffer boundaries. Lee *et al.*[24] investigated in detail the vertical size of the GaAs buffer needed to obtain vanishing hydrostatic strain at the box boundaries.

C. Atomistic tight-binding electronic structure calculation

With the equilibrium atomic positions known, we can calculate the single-particle electronic states. If we were able to carry out fully self-consistent calculations, including self-energy, we could in principle project this complicated many-body problem into a single-particle Hamiltonian of noninteracting quasiparticles. Since we do not know this effective Hamiltonian, we expand the single particle wave function as a linear combination of atomic orbitals (LCAO),

$$\phi = \sum_{\vec{R},\alpha} c_{\vec{R}\alpha}|\vec{R}\alpha\rangle, \quad (2)$$

and parametrize the Hamiltonian in a tight-binding form, which written in the language of the second quantization reads,

$$\hat{H}_{\mathrm{TB}} = \sum_{i=1}^{N}\sum_{\alpha=1}^{20}\epsilon_{i\alpha}c_{i\alpha}^{+}c_{i\alpha} + \sum_{i=1}^{N}\sum_{\alpha=1,\beta=1}^{20}\lambda_{i\alpha,\beta}c_{i\alpha}^{+}c_{i\beta} + \sum_{i=1}^{N}\sum_{j=1}^{4}\sum_{\alpha,\beta=1}^{20} t_{i\alpha,j\beta}c_{i\alpha}^{+}c_{j\beta}. \quad (3)$$

Here N is the number of atoms, $c_{i\alpha}^{+}$ ($c_{i\alpha}$) are the creation (annihilation) operators of a carrier on the orbital α localized on the site i, $\epsilon_{i\alpha}$ is the corresponding on-site energy, and $t_{i\alpha,j\beta}$ describes the hopping of the particle between orbitals on the given atom and those on the four neighboring sites. Coupling to farther neighbors is neglected. Finally, $\lambda_{i\alpha,\beta}$ accounts for the spin-orbit interaction.[25] Spin-orbit type coupling between d type orbitals is neglected. In our tight-binding approach each atom is assigned ten valence orbitals: one s, three p, five d, and an additional s^* orbital accounting for higher-lying states. Each orbital is doubly spin degenerate, thus resulting in the 20 bands model. Hopping matrix elements $t_{i\alpha,j\beta}$ are expressed as geometric functions of two-center integrals and depend only on the relative positions of the atoms i and j.[26] This approach limits the number of unknown matrix elements as they can be related via Slater–Koster rules to a relatively small subset of two-center integrals $V_{\alpha\beta,\gamma}$. The tight-binding parameters E_α, $\lambda_{\alpha,\beta}$, and $V_{\alpha\beta,\gamma}$ are obtained by fitting bulk band structure to the experimentally known band gaps and effective masses at high symmetry points of the Brillouin zone using a genetic algorithm.[27–30]

All the complicated details, including treatment of the interface between InAs and GaAs, treatment of dangling bonds appearing on the surface of the finite computational domain[24] will be presented in future more detailed report on QNANO.

D. Strain effects in the tight-binding Hamiltonian

To account for the effect of changes in tight-binding parameters due to the strain-induced changes in bond lengths, we use a generalized version of the Harrison's law:[31] $V_{\alpha\beta,\gamma} = V^0_{\alpha\beta,\gamma}(d_{ij}/d_0)^{\eta}$, where $V^0_{\alpha\beta,\gamma}$ is the two-center integral for the unstrained case, d_{ij}/d_0 is the ratio of the new to old (ideal) bond length d, and η is the scaling exponent to be discussed later. Modified $V_{\alpha\beta,\gamma}$ are used to build the tight-binding Hamiltonian for the strained system. The changes in bond angles, on the other hand, are accounted for automatically via the Slater–Koster rules.

Finally, following Boykin *et al.*[29] and Jancu *et al.*,[27] we introduce the following modification of on-site (diagonal) matrix elements due to strain:

$$\epsilon_{\vec{R}\alpha} = \epsilon^0_{\vec{R}\alpha} + \sum_{\vec{R}\in nn}\sum_{\beta}\left[C_{\vec{R}\alpha,\vec{R}'\beta}\frac{(t^0_{\vec{R}\alpha,\vec{R}'\beta})^2 - (t_{\vec{R}\alpha,\vec{R}'\beta})^2}{\epsilon^0_{\vec{R}\alpha} + \epsilon^0_{\vec{R}'\beta}}\right], \quad (4)$$

where C are empirical material parameters to be determined.

We fit the parameters η and C to match evolution of bulk band edges given by Bir–Pikus model with experimentally measured deformation potentials for the case of hydrostatic strain. However, for the more complicated case of the biaxial strain we fit the tight-binding model to reproduce results obtained by more elaborate density functional theory calculation.[32] In order to combine those two types of strain in one set of parameters we developed a genetic algorithm that performs a simultaneous fit to both hydrostatic and biaxial strain cases.

E. Multiexciton Hamiltonian

The single-particle eigenstates ϕ_i and energies E_i do not describe the excitations of an interacting system because they do not account for the electron-electron interactions. Labeling the occupied conduction band states by "electrons" and empty valence band states by "holes," the Hamiltonian

for the interacting electrons and holes can be written in analogy to the GW-Bethe-Salpeter equation (Ref. 33) approach as[4]

$$\hat{H}_{\mathrm{ex}} = \sum_i E_i^e c_i^\dagger c_i + \sum_i E_i^h h_i^\dagger h_i + \frac{1}{2}\sum_{ijkl} V_{ijkl}^{ee} c_i^\dagger c_j^\dagger c_k c_l + \frac{1}{2}\sum_{ijkl} V_{ijkl}^{hh} h_i^\dagger h_j^\dagger h_k h_l - \sum_{ijkl} V_{ijkl}^{eh,\mathrm{dir}} c_i^\dagger h_j^\dagger h_k c_l + \sum_{ijkl} V_{ijkl}^{eh,\mathrm{exchg}} c_i^\dagger h_j^\dagger c_k h_l. \quad (5)$$

Here V_{ijkl} are Coulomb matrix elements describing the direct and exchange interactions between electrons and holes, discussed below. Unlike in the GW-BSE approach, here the self-energy contribution is assumed to be constant and already incorporated in the quasielectron and quasihole energies, which were obtained from experimental bulk gaps.

For N electrons and M holes we establish the multiexciton configurations by populating the single-particle states with carriers in all possible ways. In the example shown in Fig. 1 we restrict the single-particle orbitals to six lowest electron and six hole levels, with each level corresponding to a Kramers doublet, giving the total of 12 electron and 12 hole states. In the configuration-interaction procedure we set up the matrix of the many-body Hamiltonian in the basis of these configurations and diagonalize it numerically to obtain energies and ground and excited states of the multiexciton complexes.

In the last step of the computational procedure we compute the optical spectra by calculating the intensity of photoluminescence from the recombination of one electron-hole pair in a N-exciton state using the Fermi's Golden Rule $I(\omega)=\Sigma_f|\langle f,N-1|P^-|i,N\rangle|^2\delta(E_i-E_f-\hbar\omega)$, where $|i,N\rangle$ is ith state of the N-exciton system, and $|f,N-1\rangle$ is the fth state of the $N-1$ exciton system. The interband polarization operator P^- describes all possible electron-hole recombination processes $P^-=\Sigma_{\mathrm{lm}}\langle l_e|\vec{\epsilon}\cdot\vec{r}|m_h\rangle c_l h_m$ where $\langle l_e|\vec{\epsilon}\cdot\vec{r}|m_h\rangle$ is the dipole matrix element calculated using single-particle tight-binding wave functions for a given polarization of light $\vec{\epsilon}$.

F. Coulomb and dipole matrix elements

With length and energy measured, respectively, in the effective Bohr radius and effective Rydberg computed for the quantum dot material, the Coulomb matrix elements V_{ijkl} are given as

$$V_{ijkl} = \int d\vec{r}_1 \int d\vec{r}_2 \phi_i^*(\vec{r}_1)\phi_j^*(\vec{r}_2) \times \frac{2}{\epsilon(\vec{r}_1,\vec{r}_2)|\vec{r}_1-\vec{r}_2|}\phi_k(\vec{r}_2)\phi_l(\vec{r}_l), \quad (6)$$

where $\epsilon(\vec{r}_1,\vec{r}_2)$ is the position-dependent dielectric function. Substituting LCAO form of ϕ and retaining only two-center contributions gives

$$V_{ijkl} = \sum_{\vec{R}_1}\sum_{\vec{R}_2}\sum_{\alpha_1\alpha_2\alpha_3\alpha_4} c^{i*}_{\vec{R}_1\alpha_1} c^{j*}_{\vec{R}_1\alpha_1} c^{k}_{\vec{R}_1\alpha_1} c^{l}_{\vec{R}_1\alpha_1} \times \langle \vec{R}_1\alpha_1,\vec{R}_2\alpha_2|\frac{2}{\epsilon(\vec{r}_1,\vec{r}_2)|\vec{r}_1-\vec{r}_2|}|\vec{R}_2\alpha_3,\vec{R}_1\alpha_4\rangle. \quad (7)$$

To proceed further we need to assume a functional form of the dielectric function. In our treatment we assume the dielectric function to be constant and equal to the dielectric constant ϵ of the material for distances equal or greater than the nearest-neighbor distance, and equal to 1 for shorter distances. Further, we make use of the orthogonality of the atomic orbitals and assume that for sites which are apart from each other the exact structure of the localized orbitals is not important.[6] These assumptions yield approximate Coulomb matrix elements in the form

$$V_{ijkl} = \sum_{\vec{R}_1}\sum_{\vec{R}_2\neq\vec{R}_1}\left[\sum_{\alpha_1} c^{i*}_{\vec{R}_1\alpha_1} c^{l}_{\vec{R}_1\alpha_1}\right] \times \left[\sum_{\alpha_2} c^{j*}_{\vec{R}_2\alpha_2} c^{k}_{\vec{R}_2\alpha_2}\right]\frac{2}{\epsilon|\vec{R}_1-\vec{R}_2|} + \sum_{\vec{R}_1}\sum_{\alpha_1\alpha_2\alpha_3\alpha_4} c^{i*}_{\vec{R}_1\alpha_1} c^{j*}_{\vec{R}_1\alpha_1} c^{k}_{\vec{R}_1\alpha_1} c^{l}_{\vec{R}_1\alpha_1} \times \langle \vec{R}_1\alpha_1,\vec{R}_1\alpha_2|\frac{2}{|\vec{r}_1-\vec{r}_2|}|\vec{R}_1\alpha_3,\vec{R}_1\alpha_4\rangle. \quad (8)$$

The first term is the long-range contributions built from the monopole interaction of two charge densities localized at different atomic sites. The second term is the on-site part calculated by direct integration with atomic orbitals. Following Refs. 7 and 8 for the purpose of this calculation we approximate the tight-binding orbitals with atomic Slater orbitals.

Using similar assumptions as to the orthogonality of the orbitals we compute the dipole matrix elements (in this case for light polarized along x direction) as,[6,34]

$$\langle\phi_e|x|\phi_h\rangle = \sum_{\vec{R}\alpha} R_x c^{e*}_{\vec{R}\alpha} c^{h}_{\vec{R}\alpha} + \sum_{\vec{R}\alpha}\sum_{\beta\neq\alpha} c^{e*}_{\vec{R}\alpha} c^{h}_{\vec{R}\beta}\langle\alpha|x|\beta\rangle + \sum_{\vec{R}_1\alpha}\sum_{\vec{R}_2\neq\vec{R}_1\beta} c^{e*}_{\vec{R}_1\alpha} c^{h}_{\vec{R}_2\beta}\langle\vec{R}_1\alpha|x|\vec{R}_2\beta\rangle, \quad (9)$$

where the first sum gives the "volume" contribution determined by the position of each atom $\vec{R}=(R_x,R_y,R_z)$. The second term is built from intra-atomic dipole moments for atomic transitions between orbitals on the same atom and the last term are contributions coming from orbitals centered on different atoms. As in the case of Coulomb matrix elements we use Slater orbitals[30] to calculate intra- and interatomic dipole elements.

G. Single particle levels of lens-shaped and indium-flushed InAs dots

We present here results of calculations of single-particle levels of a lens shaped, InAs dot, shown in Fig. 2(a), and an InAs dot grown using the indium-flush technique,[21] shown in Fig. 2(c). The height of the lens is $h=5$ nm and the base diameter $D=12.5$ nm. Figure 2(b) shows the charge distribution and energies corresponding to a few lowest electron

and hole levels. We see that the energies and envelope wave functions of electronic states are well described by the *s*, *p*, and *d* energy shells of a two-dimensional harmonic oscillator.[35] However, surprisingly, the hole energy levels cannot be grouped into quasidegenerate shells.

Figure 2(c) shows the structure of the same dot but grown using the indium-flush technique developed by Wasilewski *et al.*[21] The height of this disklike dot is now $D=2$ nm. We see that the energies and envelope wave functions of electronic states are again well described by the *s*, *p*, and *d* energy shells of a two-dimensional harmonic oscillator. However, in these structures the hole energy levels also can be grouped into quasidegenerate shells. This conclusion is in excellent agreement with the harmonic oscillator spectrum measured on indium-flush grown quantum dots.[12] This example points to the nontrivial role of shape, composition, strain, and spin-orbit interaction in designing electronic properties of quantum dots.

H. Multiexciton spectra and hidden symmetry

As already mentioned, the indium-flush grown quantum dots show degenerate electronic shells for both the electrons and holes. Filling of those degenerate shells is controlled by electron-electron, hole-hole, and electron-hole interactions according to hidden symmetries. Figure 1 shows the emission spectra from multiexciton complexes as a function of the number of excitons, i.e., showing the filling of degenerate shells, in indium-flush grown dot identical to the one shown in Fig. 2(c) but with diameter $D=10$ nm. We see that the emission from the *s* shell and *p* shells is not a sensitive function of the filling of the shell. The small structure in the *p* shell is related to total spin and scattering to higher shells. The associated emission structure in the *s* shell energy range is not related to hidden symmetries and is a sensitive function of the filling of the shell, in agreement with results obtained using the effective-mass harmonic oscillator states.[13]

III. CONCLUSIONS

In conclusion, we have reviewed our calculations of the electronic and optical structure of SADs based on several models of their single-particle properties. In each case the single-particle energies and states were used to construct the matrix elements of the many-body Hamiltonian in the configuration-interaction approach. First, treating the electrons and holes in the single-band effective-mass approach we have established the hidden symmetries, governing the filling of degenerate shells by excitons. These symmetries are responsible for the insensitivity of emission spectra from such a shell to the filling of that shell. However, they apply only when the carriers are allowed to relax to form the ground state of the system. If the state of the system is chosen, e.g., by injecting spin-polarized electrons into the dot, the emission spectra are found to depend very strongly both on the filling of the shell and the polarization of the carriers. We have also demonstrated that the multiexciton emission spectra, and in particular, the biexciton-exciton cascade, can be tuned by applying an external electric field in the plane of the dot. We have shown that in vertically coupled double dot systems the single-band treatment of holes is not sufficient. In these systems the spin-orbit interaction responsible for the mixing of valence subbands is strong enough to lead to the crossing of the bonding and antibonding quantum molecular hole levels as a function of the distance between dots, and to the antibonding character of the ground hole state for larger dot separations.

We account for all the effects of subband mixing, shape, size, and atomistic structure of the system in the atomistic tight-binding calculation of quantum dot states carried out with the QNANO tool. In this procedure we define the geometry of the sample on an atomistic level and relax the atomic positions to minimize the total elastic energy. The single-particle energies and states are further computed by setting up and diagonalizing the 20-band $sp^3d^5s^*$ tight-binding Hamiltonian in the nearest-neighbor approximation. The resulting wave functions are used to compute the Coulomb matrix elements utilized further in the configuration-interaction Hamiltonian and the dipole elements needed to find the emission spectra. On the example of the lens-shaped and indium-flushed SADs we indicated that the single-particle spectra can be engineered by the size, shape, strain, and composition of the system. Finally, based on the atomistic calculations we confirmed the validity of the hidden symmetries obtained earlier in the single-band effective-mass picture.

ACKNOWLEDGMENTS

The authors thank QuantumWorks and Canadian Institute for Advanced Research for financial support.

[1] P. Hawrylak and M. Korkusinski, in *Single Quantum Dots: Fundamentals, Applications, and New Concepts, Topics in Applied Physics*, Vol. 90, edited by P. Michler, (Springer, New York, 2003).
[2] L. Jacak, P. Hawrylak, and A. Wojs, *Quantum Dots* (Springer, Berlin, 1998).
[3] D. Bimberg, M. Grundmann, and N. N. Ledentsov, *Quantum Dot Heterostructures* (Wiley, New York, 1998).
[4] W. Sheng, S.-J. Cheng, and P. Hawrylak, Phys. Rev. B **71**, 035316 (2005).
[5] W. Sheng and P. Hawrylak, Phys. Rev. B **72**, 035326 (2005).
[6] S. Schulz, S. Schumacher, and G. Czycholl, Phys. Rev. B **73**, 245327 (2006).
[7] S. Lee, L. Jönsson, J. W. Wilkins, G. W. Bryant, and G. Klimeck, Phys. Rev. B **63**, 195318 (2001).
[8] K. Leung and K. B. Whaley, Phys. Rev. B **56**, 7455 (1997).
[9] R. Santoprete, P. Kratzer, M. Scheffler, R. B. Capaz, and B. Koiller, J. Appl. Phys. **102**, 023711 (2007).
[10] A. Canning, L. W. Wang, A. Williamson, and A. Zunger, J. Comput. Phys. **160**, 29 (2000).
[11] G. Bester and A. Zunger, Phys. Rev. B **71**, 045318 (2005).
[12] S. Raymond, S. Studenikin, A. Sachrajda, Z. Wasilewski, S. J. Cheng, W. Sheng, P. Hawrylak, A. Babinski, M. Potemski, G. Ortner, and M. Bayer, Phys. Rev. Lett. **92**, 187402 (2004).
[13] P. Hawrylak, Phys. Rev. B **60**, 5597 (1999).
[14] M. Bayer, O. Stern, P. Hawrylak, S. Fafard, and A. Forchel, Nature (London) **405**, 923 (2000).
[15] M. Korkusinski and P. Hawrylak, Phys. Rev. Lett. **101**, 027205 (2008).
[16] M. Korkusinski, P. Hawrylak, and M. Potemski, J. Phys. Condens. Matter **20**, 454213 (2008).
[17] M. Korkusinski, M. Reimer, R. Williams, and P. Hawrylak, Phys. Rev. B **79**, 035309 (2009).
[18] M. E. Reimer, M. Korkusinski, D. Dalacu, J. Lefebvre, J. Lapointe, P. J. Poole, G. C. Aers, W. R. McKinnon, P. Hawrylak, and R. L. Williams, Phys. Rev. B **78**, 195301 (2008).
[19] J. I. Climente, M. Korkusinski, G. Goldoni, and P. Hawrylak, Phys. Rev. B **78**, 115323 (2008).

[20]W. Jaskólski, M. Zieliński, G. W. Bryant, and J. Aizpurua, Phys. Rev. B **74**, 195339 (2006).
[21]Z. R. Wasilewski, S. Fafard, and J. P. McCaffrey, J. Cryst. Growth **201–202**, 1131 (1999).
[22]P. N. Keating, Phys. Rev. **145**, 637 (1966); R. M. Martin, Phys. Rev. B **1**, 4005 (1970).
[23]C. Pryor, J. Kim, L. W. Wang, A. J. Williamson, and A. Zunger, J. Appl. Phys. **83**, 2548 (1998); M. Tadić, F. M. Peeters, K. L. Janssens, M. Korkusinski, and P. Hawrylak, *ibid.* **92**, 5819 (2002).
[24]S. Lee, F. Oyafuso, P. von Allmen, and G. Klimeck, Phys. Rev. B **69**, 045316 (2004).
[25]D. J. Chadi, Phys. Rev. B **16**, 790 (1977).
[26]J. C. Slater and G. F. Koster, Phys. Rev. **94**, 1498 (1954).
[27]J. M. Jancu, R. Scholz, F. Beltram, and F. Bassani, Phys. Rev. B **57**, 6493 (1998).
[28]G. Klimeck, R. C. Bowen, T. B. Boykin, and T. A. Cwik, Superlattices Microstruct. **27**, 519 (2000).
[29]T. B. Boykin, G. Klimeck, R. C. Bowen, and F. Oyafuso, Phys. Rev. B **66**, 125207 (2002).
[30]J. G. Diaz and G. W. Bryant, Phys. Rev. B **73**, 075329 (2006).
[31]W. A. Harrison, *Electronic Structure and the Properties of Solids* (Freeman, New York, 1980).
[32]P. R. C. Kent, G. L. W. Hart, and A. Zunger, Appl. Phys. Lett. **81**, 4377 (2002).
[33]C. Spataru, S. Ismail-Beigi, L. X. Benedict, and S. G. Louie, Phys. Rev. Lett. **92**, 077402 (2004).
[34]G. W. Bryant and W. Jaskólski, Phys. Rev. B **67**, 205320 (2003).
[35]P. Hawrylak, Phys. Rev. Lett. **71**, 3347 (1993).